Journal of Statistical Physics, Vol. 62, Nos. 5/6, 1991

A Lattice Gas Model for Thermohydrodynamics

Shiyi Chen,[1,2] Hudong Chen,[1,3] Gary D. Doolen,[1] Semion Gutman,[1] and Minxu Lee[1]

Received May 21, 1990; final October 27, 1990

The lattice gas model is extended to include a temperature variable in order to study thermohydrodynamics, the combination of fluid dynamics and heat transfer. The compressible Navier–Stokes equations are derived using a Chapman–Enskog expansion. Heat conduction and convection problems are investigated, including Bénard convection. It is shown that the usual rescaling procedure can be avoided by controlling the temperature.

KEY WORDS: Lattice gas; thermohydrodynamics; Bénard convection; Galilean invariance.

1. INTRODUCTION

Lattice gas automata were first proposed by Frisch, Hasslacher, and Pomeau (FHP)[1] to simulate incompressible Navier–Stokes equations. As a parallel and powerful computational method, the lattice gas scheme has been extended to describe additional fluid problems, including flow through porous media, chemical reactions,[3,4] phase transitions,[5,6] and surface tension.[7] Lattice gas automata are classical many-body dynamical systems which provide several simple solvable models to study classical statistical problems. Recent achievements in this area include the derivation of wavelength dependence and frequency dependence of the transport coefficients[8] and long-time behavior of the velocity autocorrelation

[1] Center for Nonlinear Studies, Los Alamos National Laboratory, Los Alamos, New Mexico 87545.

[2] Current address: Bartol Research Institute, University of Delaware, Newark, Delaware 19716.

[3] Current address: Department of Physics and Astronomy, Dartmouth College, Hanover, New Hampshire 03755.

0022-4715/91/0300-1121$06.50/0

functions.[9] Most research using lattice gas methods has focused on flow problems, particularly on isothermal flows.

In this paper, we propose a lattice gas model incorporating 13 lattice gas velocities to simulate a more realistic thermohydrodynamic system. The model has a definition of temperature which is related to the microscopic kinetic energy. A Chapman–Enskog expansion is used to derive the thermohydrodynamic equations, Eq. (45), and the transport coefficients, Eqs. (43) and (44). The FHP[1,2] lattice gas requires a scaling of time, pressure, and viscosity because of the non-Galilean invariance. Our model can avoid this scaling for isothermal systems.

In Section 2, we describe the model, discuss its thermodynamic properties, and derive the thermohydrodynamic equations for local equilibrium. The derivation of transport coefficients is given in Section 3. Applications of this model to heat conduction in channel flows are studied in Section 4. Section 5 presents computer simulation results for Bénard convection. In Section 6, we discuss the isothermal limit and the partial recovery of the Galilean invariance. The last section discusses future applications.

An earlier model including temperature was proposed by Burgess and Zaleski,[10] in which "colors" are used to represent an energy variable. Even though simulations of this model exhibit interesting phenomena, the model is unrealistic. The colors are particle labels which have no intrinsic relation to the dynamical properties. The propagation of thermal energy is represented by the color field. The model does not possess a well-defined thermodynamic energy nor temperature transfer. The transport coefficients can only depend on density. In physical systems, the transport coefficients depend on both density and temperature.

2. A LATTICE GAS MODEL FOR THERMOHYDRODYNAMICS

For single-speed lattice gas models, such as six-bit lattice gas models,[1,2,11] the energy equation is equivalent to the continuity equation. For seven-bit lattice gas models with rest particles,[12] local kinetic energy is not conserved during some collision processes. Therefore, it is necessary to include at least two different nonzero particle speeds in the model to study temperature-dependent effects. In this paper, we construct a lattice gas model with three types of particles, distinguished by their speeds and masses. We assume these particles have the speed zero, one, and two, with masses $m_\sigma = 2/3$, 1, and 1/2, respectively, where σ ($=0$, 1, or 2) denotes the type of particle.

The reason for using different masses is to maximize the number of allowed collisions while conserving mass, momentum, and energy exactly.

Having both moving masses have the same momentum greatly increases the number of allowed collisions. Maximizing the number of collisions increases the allowed range of Reynolds numbers. Having a mass of 2/3 for the stopped particle maximizes the number of particle-changing collisions.

The spatial lattice is triangular. At each lattice site, there are 12 different nonzero velocity states and one zero-speed state allowed. Each velocity is designated by $\mathbf{e}_a^\sigma = c_\sigma[\cos(2\pi a/6), \sin(2\pi a/6)]$ ($a = 1,..., 6$; $c_\sigma = 0$, 1, and 2). As mentioned above, both speed-one and speed-two particles are chosen to have unit momentum in order to maximize the number of momentum-conserving collisions. We define ε_a^σ as the kinetic energy for a type σ particle divided by its mass. Then $\varepsilon_a^\sigma = \frac{1}{2}|\mathbf{e}_a^\sigma|^2$ and the corresponding values associated with the particles are zero, one-half, and one, respectively. In order to minimize computer memory requirements, an exclusion rule is imposed which forbids two particles of the same type to occupy a given velocity direction at a site. Unlike the passive scalar model,[13] we allow two particles with different speeds to occupy a given velocity direction at a site.

We use $N_a^\sigma(\mathbf{x}, t)$ ($\sigma = 0, 1, 2$; $a = 1,..., 6$) to denote the particle occupation at site $\mathbf{x}$ and time t. We have $N_a^\sigma = 0$ or 1.

There are two microscopic processes: streaming and collision. In the streaming process, a particle in state $\mathbf{e}_a^\sigma$ either stays at its original site or moves from its present site to the nearest or next nearest neighbor site in the direction $\mathbf{e}_a^\sigma$, depending on its speed (zero, one, or two lattice units per unit time). There are no particle interactions during streaming processes. When particles occupy the same site, a collision can occur, changing particle directions and speeds. Examples of allowed collisions are shown in Fig. 1.

In general, three kinds of collisions are allowed. The first kind of collision includes collisions between the same type of particles. Collision rules for speed-one particles[1] are the same as the rules for speed-two particles. The second kind of collision involves both speed-one and speed-two particles and conserves the number of particles of each type. The third kind of collision involves both speed-one and speed-two particles and allows a change in the number of each type of particle. An example is shown in Fig. 1c: a speed-two particle collides with a rest particle and two speed-one particles emerge. Only this type of collision can change the number of zero-speed particles. To increase the number of this type of collision, we allow all possible collisions which conserve total mass, momentum, and energy.

These three kinds of collisions can occur simultaneously or sequentially (there is no difference for a complete collision table). For simultaneous collisions, there is no order of preference for the collisions. One simply takes the entry particle configuration and redistributes par-

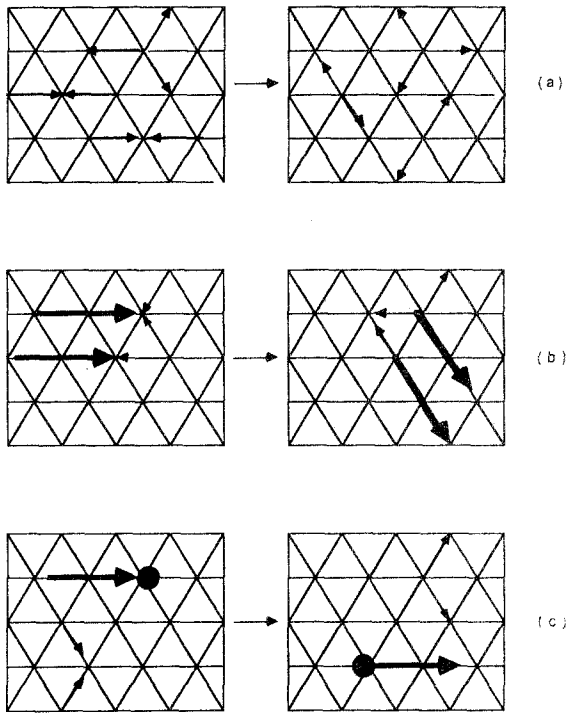

Fig. 1. Some collision rules for the 13-bit lattice gas model. The length of the arrows is proportional to speed. Speed-one particles have a unit mass. Speed-two particles have 1/2 unit mass. The left side refers to the states before a collision. The right side refers to the states after the collision. (a) Collisions between the same type of particles; (b) collisions between different types; (c) collisions which change the number of each type of particle.

ticles, following the conservation rules. This usually requires a large collision table. For a system with m discrete velocities, a table with 2^m entries is required. Sequential collisions, however, can split the collision time into an arbitrary number of time steps with one kind of collision occurring during each substep. Each collision uses the present particle distributions and requires fewer bits to describe collisions. For example, we can have the first kind of collision for speed-one and speed-two particles as shown in Fig. 1. Then we can use the updated particles as input for the second kind of collision. Finally, we can use these updated particles as input for the third kind of collision. We will discuss the macroscopic difference between simultaneous collisions and sequential collisions later.

The kinetic equation for the particle occupation N_a^σ due to collision and streaming operations can be written

$$N_a^\sigma(\mathbf{x}+\mathbf{e}_a^\sigma, t+1) - N_a^\sigma(\mathbf{x}, t) = \Lambda_a^\sigma \tag{1}$$

where A_a^σ is the collision operator for N_a^σ. Let $f_a^\sigma = \langle N_a^\sigma \rangle$ be the ensemble-averaged particle distribution, where $\langle \cdot \rangle$ represents the ensemble average. Assume that the collision time scale is much shorter than the characteristic time and that the lattice length is much smaller than the characteristic spatial scale of the hydrodynamics in which we are interested. Then we can rewrite Eq. (1) in the following form:

$$\frac{\partial f_a^\sigma}{\partial t} + \mathbf{e}_a^\sigma \cdot \nabla f_a^\sigma = \Omega_a^\sigma \tag{2}$$

where Ω_a^σ represents the rate of change of f_a^σ due to collisions. To obtain Eq. (2), we have used a Boltzmann approximation in which we assume there is no correlation between different particle states at the same site and the same time, i.e.,

$$\langle N_a^\sigma(\mathbf{x}, t)\, N_b^\beta(\mathbf{x}, t) \rangle = \langle N_a^\sigma(\mathbf{x}, t) \rangle \langle N_b^\beta(\mathbf{x}, t) \rangle$$

We define the macroscopic mass density n, fluid momentum field $n\mathbf{u}$, and particle internal energy $n\varepsilon$ by the following equations:

$$\sum_{a,\sigma} m_\sigma f_a^\sigma = n \tag{3}$$

$$\sum_{a,\sigma} m_\sigma f_a^\sigma \mathbf{e}_a^\sigma = n\mathbf{u} \tag{4}$$

$$\sum_{a,\sigma} m_\sigma f_a^\sigma (\mathbf{e}_a^\sigma - \mathbf{u}) \cdot (\mathbf{e}_a^\sigma - \mathbf{u}) = n\varepsilon \tag{5}$$

We define the temperature T of the lattice gas using

$$\varepsilon = \frac{i}{2} k_B T \tag{6}$$

where i is the number of degrees of freedom and k_B is the Boltzmann constant. This is in analogy to the classical equipartition theorem. ε is an intensive quantity, which we use to represent temperature in this paper. This definition of temperature is a kinetic definition which differs from a thermodynamic definition. Because the kinetic energy for lattice gas particles is bounded, our temperature range is also bounded. A thermodynamic definition of temperature is also possible which has the usual infinite range. The choice of definition of temperature affects the pressure definition. Pressures obtained using a kinetic definition can differ from pressures obtained using a thermodynamic definition. Results of using either choice of definition can be related to the results of the other choice.

Conservation of mass, momentum, and energy require the following constraints on the collision operator:

$$\sum_{a,\sigma} m_\sigma \Omega_a^\sigma = 0, \qquad \sum_{a,\sigma} m_\sigma \Omega_a^\sigma \mathbf{e}_a^\sigma = 0$$
$$\sum_{a,\sigma} m_\sigma \Omega_a^\sigma (\mathbf{e}_a^\sigma)^2 = 0 \tag{7}$$

Taking moments of (2), we obtain the following continuity, momentum and energy equations:

$$\frac{\partial n}{\partial t} + \nabla \cdot n\mathbf{u} = 0 \tag{8}$$

$$\frac{\partial n\mathbf{u}}{\partial t} + \nabla \cdot \hat{\Pi} = 0 \tag{9}$$

$$\frac{\partial (n\varepsilon)}{\partial t} + \nabla \cdot (n\varepsilon \mathbf{u}) + \nabla \cdot \mathbf{q} + 2\hat{P} : \nabla \mathbf{u} = 0 \tag{10}$$

where $\hat{\Pi}$ is the symmetric tensor of order 2, $\hat{\Pi}_{\alpha\beta} = \sum_{a,\sigma} m_\sigma f_a^\sigma (\mathbf{e}_a^\sigma)_\alpha (\mathbf{e}_a^\sigma)_\beta$, $\mathbf{q}$ is the heat flux, $(\mathbf{q})_\alpha = \sum_{a,\sigma} m_\sigma f_a^\sigma (\mathbf{e}_a^\sigma - \mathbf{u})^2 (\mathbf{e}_a^\sigma - \mathbf{u})_\alpha$, and $\hat{P}$ is the pressure tensor, $\hat{P}_{\alpha\beta} = \sum_{a,\sigma} m_\sigma f_a^\sigma (\mathbf{e}_a^\sigma - \mathbf{u})_\alpha (\mathbf{e}_a^\sigma - \mathbf{u})_\beta$.

To obtain hydrodynamic equations, we assume the system approaches a local thermodynamic equilibrium. In the Chapman Enskog expansion, the equilibrium state corresponds to the zeroth-order collision term in the kinetic equation (2), i.e., $\Omega_a^{\sigma(0)} = 0$. This leads to a Fermi Dirac equilibrium distribution

$$f_a^{\sigma(0)} = \frac{1}{1 + \exp[m_\sigma(\alpha + \beta \mathbf{e}_a^\sigma \cdot \mathbf{u} + \gamma \varepsilon_a^\sigma)]} \tag{11}$$

where α, β, and γ are Lagrange multipliers determined by the definitions (3)–(5). α, β, and γ are functions of n, $\mathbf{u}$, and ε.

To obtain solutions for $\hat{\Pi}$, $\mathbf{q}$, and $\hat{P}$, we expand $f_a^{\sigma(0)}$ to third order in u, assuming $|\mathbf{u}| \ll 1$ and expand, obtaining $\alpha = \alpha_0 + \alpha_1 u^2$, $\beta = \beta_0 + \beta_1 u^2$, and $\gamma = 2(\gamma_0 + \gamma_1 u^2)$. The velocity expansion of $f_a^{\sigma(0)}$ then has the form

$$\begin{aligned} f_a^{\sigma(0)} = {} & d_a^\sigma - d_a^\sigma (1 - d_a^\sigma)[m_\sigma \beta_0 \mathbf{e}_a^\sigma \cdot \mathbf{u} + m_\sigma(\alpha_1 + \gamma_1 |\mathbf{e}_a^\sigma|^2) u^2] \\ & + \frac{d_a^\sigma}{2}(1 - d_a^\sigma)(1 - 2d_a^\sigma) m_\sigma^2 \beta_0^2 (\mathbf{e}_a^\sigma \cdot \mathbf{u})^2 \\ & - d_a^\sigma (1 - d_a^\sigma) m_\sigma \beta_1 (\mathbf{e}_a^\sigma \cdot \mathbf{u}) u^2 \\ & + d_a^\sigma (1 - d_a^\sigma)(1 - 2d_a^\sigma) m_\sigma^2 \beta_0 (\alpha_1 + \gamma_1 |\mathbf{e}_a^\sigma|^2)(\mathbf{e}_a^\sigma \cdot \mathbf{u}) u^2 \\ & - \frac{1}{6} d_a^\sigma (1 - d_a^\sigma)(1 - 6d_a^\sigma + 6d_a^{\sigma 2}) m_\sigma^3 \beta_0^3 (\mathbf{e}_a^\sigma \cdot \mathbf{u})^3 + \cdots \end{aligned} \tag{12}$$

where d_a^σ is the equilibrium distribution for $\mathbf{u}=0$,

$$d_a^\sigma = \frac{1}{1+\exp[m_\sigma(\alpha_0 + 2\gamma_0 \varepsilon_a^\sigma)]} \tag{13}$$

Because d_a^σ is independent of a, we replace d_a^σ by d_σ and ε_a^σ by ε_σ. The coefficients β_0, β_1, α_1, and γ_1 in Eq. (12) are functions of n and ε, determined by the definitions (3)–(5). Defining M to be the number of distinct velocity directions excluding zero velocity (six for a hexagonal lattice), and defining D to be the spatial dimension (two for our model),

$$\beta_0 = -\frac{n}{(M/D)\sum_\sigma d_\sigma(1-d_\sigma)\, m_\sigma^2 c_\sigma^2}$$

$$\alpha_1 = \frac{a_3 b_2 - a_2 b_3}{a_1 b_2 - a_2 b_1}$$

$$\gamma_1 = \frac{a_1 b_3 - a_3 b_1}{a_1 b_2 - a_2 b_1}$$

$$\beta_1 = \frac{1}{\sum_\sigma m_\sigma^2 d_\sigma(1-d_\sigma)\, c_\sigma^2}\left\{\beta_0\left[\sum_\sigma m_\sigma^3 d_\sigma(1-2d_\sigma)(\alpha_1+\gamma_1 c_\sigma^2)\, c_\sigma^2\right]\right.$$
$$\left. -\frac{\beta_0^2(d+1)}{6(d+2)}\left[\sum_\sigma m_\sigma^4 d_\sigma(1-d_\sigma)(1-6d_\sigma+6d_\sigma^2)\, c_\sigma^4\right]\right\}$$

In the above equations,

$$a_1 = M\sum_\sigma m_\sigma^2 d_\sigma(1-d_\sigma)$$

$$a_2 = M\sum_\sigma m_\sigma^2 d_\sigma(1-d_\sigma)\,\varepsilon_\sigma$$

$$a_3 = \frac{\beta_0^2}{2}\frac{M}{D}\sum_\sigma m_\sigma^3 d_\sigma(1-d_\sigma)(1-2d_\sigma c_\sigma^2)$$

$$b_1 = a_2$$

$$b_2 = M\sum_\sigma m_\sigma^2 d_\sigma(1-d_\sigma)\,\varepsilon_\sigma^2$$

$$b_3 = \frac{\beta_0^2}{2}\frac{M}{D}\sum_\sigma m_\sigma^3 d_\sigma(1-d_\sigma)(1-2d_\sigma)\, c_\sigma^2\varepsilon_\sigma - \frac{2}{n}$$

For models in which the rest particle does not have internal energy, we obtain

$$\hat{\Pi}_{\alpha\beta}^{(0)} = ng(n,\varepsilon)\, u_\alpha u_\beta + p\delta_{\alpha\beta} \tag{14}$$

where $\delta_{\alpha\beta}$ is the Kronecker symbol; $g(n, \varepsilon)$ is the coefficient of the convective term,

$$g(n, \varepsilon) = \frac{\beta_0^2 M}{D(D+2)n} \sum_\sigma m^{\sigma 3} d_\sigma (1 - d_\sigma)(1 - 2d_\sigma)\, c_\sigma^4 \tag{15}$$

and

$$p = p_0 + p_1 u^2 \tag{16}$$

Here,

$$p_0 = \sum_\sigma m_\sigma d_\sigma c_\sigma^2 \frac{M}{D} = n\varepsilon \tag{17}$$

and

$$p_1 = \frac{n}{2}[1 - g(n, \varepsilon)] \tag{18}$$

In Eq. (18), note that $p_1 = 0$ when $g(n, \varepsilon) = 1$. This very desirable coincidence is a direct result of including an additional speed in the model.

Equation (17) is the equation of state for an ideal gas. The sound speed c_s is $\sqrt{\varepsilon}$ for the isothermal case.

To order u^2, the heat flux vector $q_i^{(0)}$ for the equilibrium distribution $f_a^{\sigma(0)}$ is

$$q_i^{(0)} = h(n, \varepsilon)\, n\varepsilon u_i \tag{19}$$

where

$$h(n, \varepsilon) = \frac{D}{2M} \frac{n \sum_\sigma m_\sigma d_\sigma (1 - d_\sigma)\, c_\sigma^4}{(\sum_\sigma m_\sigma d_\sigma (1 - d_\sigma)\, c_\sigma^2)(\sum_\sigma m_\sigma d_\sigma c_\sigma^2)} - 2$$

and $\hat{P} : \nabla \mathbf{u} = p \nabla \cdot \mathbf{u}$. Hence, we have the first-order momentum and energy equations:

$$\begin{aligned} \partial_t (n\mathbf{u}) + \nabla \cdot (n g(n, \varepsilon)\, \mathbf{uu}) &= -\nabla p \\ \partial_t (n\varepsilon) + \nabla \cdot (n\varepsilon \mathbf{u}) &= -\nabla \cdot (nh(n, \varepsilon)\, \varepsilon \mathbf{u}) - p \nabla \cdot \mathbf{u} \end{aligned} \tag{20}$$

For a continuum case with a Maxwell distribution, $q_i^{(0)}$ will vanish. To $O(u^3)$, we can have addition terms:

$$q_i^{(0)} = \chi u^2 u_i$$

and

$$\hat{P} : \nabla \mathbf{u} = n(g(n, \varepsilon) - 1)\, \mathbf{uu} : \nabla \mathbf{u}$$

where

$$\chi = \frac{M}{D} \sum_{\sigma} [\chi_\sigma^1 + \chi_\sigma^2 + \chi_\sigma^3 + \chi_\sigma^4 + \chi_\sigma^5]$$

with

$$\chi_\sigma^1 = -\beta_0^2 m_\sigma^3 \frac{d_\sigma}{2} (1 - d_\sigma)(1 - 2d_\sigma)\, c_\sigma^4$$

$$\chi_\sigma^2 = (D+2)\, m_\sigma^2 (\alpha_1 + \gamma_1 c_\sigma^2)\, c_\sigma^2$$

$$\chi_\sigma^3 = -\beta_1 m_\sigma^2 d_\sigma (1 - d_\sigma)\, c_\sigma^4$$

$$\chi_\sigma^4 = \beta_0 m_\sigma^3 d_\sigma (1 - d_\sigma)(1 - 2d_\sigma)(\alpha_1 + \gamma_1 c_\sigma^2)\, c_\sigma^4$$

$$\chi_\sigma^5 = -\frac{1}{2(D+2)} \beta_0^3 m_\sigma^4 d_\sigma (1 - d_\sigma)(1 - 6d_\sigma + 6d_\sigma^2)\, c_\sigma^6$$

Note that the FHP-I and FHP-II models are degenerate cases of Eqs. (14) and (16). After some algebra, we obtain $g(n, \varepsilon) = (3-n)/(6-n)$ and $\varepsilon = 1/2$ for FHP-I; and $g(n, \varepsilon) = 7(7-2n)/12(7-n)$ and $\varepsilon = 3/7$ for FHP-II.[12] In general, $g(n)$ and p_1 depend on density and temperature. Temperature is usually determined by the particle density ratios between different types of particles. For the special case $d_0 = d_1 = d_2 = d$, we have the explicit form

$$g = \frac{21}{32} \frac{1 - 2d}{1 - d}$$

where d is the reduced density, $d = (2/21)n$. The term $g(n)$ has a form similar to that found in FHP models.[12]

3. THE CHAPMAN–ENSKOG EXPANSION AND TRANSPORT COEFFICIENTS

At equilibrium, we have a zeroth-order distribution which satisfies

$$\Omega_a^{\sigma(0)} = 0 \tag{21}$$

The first-order equations become

$$\frac{\partial f_a^{\sigma(0)}}{\partial t} + \mathbf{e}_a^\sigma \cdot \nabla f_a^{\sigma(0)} = \Omega_a^{\sigma(1)}, \qquad \sigma = 1, 2$$

$$\frac{\partial f_0^{(0)}}{\partial t} = \Omega_0^{(1)} \tag{22}$$

Also, we have

$$
\begin{aligned}
f_0 &= f_0^{(0)} + f_0^{(1)} \\
f_a^\sigma &= f_a^{\sigma(0)} + f_a^{\sigma(1)} \\
\Omega_0^{(1)} &= C_{0,0}^{(0)} f_0^{(1)} + \sum_{a\sigma} C_{0,a\sigma}^{(0)} f_a^{\sigma(1)} \\
\Omega_a^{\sigma(1)} &= C_{a\sigma,0}^{(0)} f_0^{(1)} + \sum_{b\lambda} C_{a\sigma,b\lambda}^{(0)} f_b^{\lambda(1)}
\end{aligned}
\tag{23}
$$

where the tensor $C_{a\sigma,b\lambda}^{(0)}$ is the collision coefficient in $\Omega_a^{\sigma(1)}$.

Substituting (12) into (22), we obtain

$$
\frac{\partial d_0}{\partial t} = C_{0,0}^{(0)} f_0^{(1)} + \sum_{a,\sigma} C_{0,a\sigma}^{(0)} f_a^{\sigma(1)}
$$

or

$$
f_0^{(1)} = \frac{1}{C_{0,0}^{(0)}} \left(\frac{\partial d_0}{\partial t} - \sum_{a,\sigma} C_{0,a\sigma}^{(0)} f_a^{\sigma(1)} \right) \tag{24}
$$

Also, we obtain the following equation for $f_a^{\sigma(1)}$:

$$
\frac{\partial f_a^{\sigma(0)}}{\partial t} + \mathbf{e}_a^\sigma \cdot \nabla f_a^{\sigma(0)} = \frac{C_{a\sigma,0}}{C_{0,0}^{(0)}} \frac{\partial d_0}{\partial t} + \sum_{b,\lambda} \tilde{C}_{a\sigma,b\lambda}^{(0)} f_b^{\lambda(1)} \tag{25}
$$

where

$$
\tilde{C}_{a\sigma,b\lambda}^{(0)} = C_{a\sigma,b\lambda}^{(0)} - \frac{C_{a\sigma,0}}{C_{0,0}^{(0)}} C_{0,b\lambda}^{(0)}
$$

To first order in u, the left-hand side of (25) has the form

$$
\begin{aligned}
L_{ta\sigma} &= \frac{\partial d_\sigma}{\partial t} - \frac{C_{a\sigma,0}}{C_{0,0}^{(0)}} \frac{\partial d_0}{\partial t} + [-\beta_0 d_\sigma (1 - d_\sigma)\, m_\sigma c_\sigma^2 (\mathbf{e}_a \mathbf{e}_a : \nabla \mathbf{u})] + c_\sigma \mathbf{e}_a \cdot \nabla d_\sigma \\
&= \frac{1}{2} [-\beta_0 d_\sigma (1 - d_\sigma)\, m_\sigma c_\sigma^2 (2\mathbf{e}_a \mathbf{e}_a - \hat{\mathbf{I}}) : \nabla \mathbf{u}] + c_\sigma \mathbf{e}_a \cdot \nabla d_\sigma \\
&\quad + \frac{\partial d_\sigma}{\partial t} - \frac{C_{a\sigma,0}}{C_{0,0}^{(0)}} \frac{\partial d_0}{\partial t} - \frac{1}{2} \beta_0 d_\sigma (1 - d_\sigma)\, m_\sigma c_\sigma^2 \nabla \cdot \mathbf{u}
\end{aligned}
\tag{26}
$$

Here $\hat{\mathbf{I}}$ is the unit tensor. We decompose $L_{ta\sigma}$ into several parts:

$$
L_{ta\sigma} = L_{ta\sigma}(\text{visc}) + L_{ta\sigma}(\text{cond}) + L_{ta\sigma}(\nabla \cdot \mathbf{u}) \tag{27}
$$

where

$$L_{ta\sigma}(\text{visc}) = \frac{1}{2}\left[-\beta_0 d_\sigma(1-d_\sigma)\, m_\sigma c_\sigma^2(2\mathbf{e}_a\mathbf{e}_a - \hat{\mathbf{I}}\right] : \nabla\mathbf{u}$$

$$L_{ta\sigma}(\text{cond}) = c_\sigma \mathbf{e}_a \cdot \nabla d_\sigma \tag{28}$$

$$L_{ta\sigma}(\nabla\cdot\mathbf{u}) = \frac{1}{2}\left[-\beta_0 d_\sigma(1-d_\sigma)\, m_\sigma c_\sigma^2 \nabla\cdot\mathbf{u}\right]$$

We have eliminated the time-dependent terms in the above equations.

In order to obtain the transport coefficients, we need to write down the detailed collision operators and their linear expansions. We only treat the simplest case: $d_0 = d_1 = d_2 = d$.

As mentioned before, collisions can be executed simultaneously or sequentially. If we consider the lattice gas to be a finite-difference scheme, the sequential collisions are suggestive of a time split method. In our simulations, the following five-step sequential collision operation was used: (1) speed-one particle collisions with all possible configurations, regardless of speed-two and rest particles; (2) speed-two particle collisions with all possible configurations, regardless of speed-one and rest particles; (3) speed-one and speed-two particle collisions. Only two-body head-on collisions (a speed-one particle collides with a speed-two particle) have been introduced. The outgoing particle direction is 60° from the incoming direction; (4) similar collisions to those described in (3) with 120° rotation; (5) either one speed-two particle collides with one rest particle or two speed-one particles collide as shown in Fig. 1c. We allow all spectators. In (3) and (4), we also allow the collisions with spectators. Then, these two particle collisions are really four-body (particle and hole) collisions, usually having the form $f_i f_j(1-f_k)(1-f_l)$, which is much larger than the standard collision form $\prod_i f_i^{s_i}(1-f_i)^{(1-s_i)}$. Here s_i is the configuration assignment at $\mathbf{x}$. In general, if there are M sequential collisions, the collision operator in Eq. (2) can be written as

$$\begin{aligned} \Omega_a^\sigma(\mathbf{x}, t) &= \sum_{i=1}^{M} \Omega_a^{(i)\sigma}(f(i-1)) \\ f(i) &= f(i-1) + \Omega_a^{(i)\sigma}(f(i-1)) \end{aligned} \tag{29}$$

where $f(i) \equiv f(\mathbf{x}, t + i/M)$ and $\Omega^{(i)}$ is the collision operator associated with the ith substep. Let $\tilde{C}^{(i)}_{a\sigma,b\lambda}$ be the linear expansion of $\Omega_a^{(i)\sigma}$. Then, it is easy to show that $\tilde{C}^{(0)}_{a\sigma,b\lambda}$ in Eq. (25) have the form

$$C^{(0)}_{a\sigma,b\lambda} = \left[\prod_{i=1}^{M} (\hat{\mathbf{I}} + \tilde{C}^{(i)}_{a\sigma,b\lambda}) - \hat{\mathbf{I}}\right] f_b^{\lambda(1)} \tag{30}$$

The matrix product $\tilde{C}^{(i)}\tilde{C}^{(i+1)}$ is not reversible. This is related to the fact that a different collision order will give different outgoing configuration and, hence, different transport coefficients.

The collision matrices in our paper have the following form:

$$\tilde{C}^{(1)}_{a\sigma,b\lambda} = \begin{pmatrix} \omega^1 & 0 \\ 0 & 0 \end{pmatrix}$$

$$\tilde{C}^{(2)}_{a\sigma,b\lambda} = \begin{pmatrix} 0 & 0 \\ 0 & \omega^2 \end{pmatrix}$$

$$\tilde{C}^{(3)}_{a\sigma,b\lambda} = \begin{pmatrix} \omega^3_1 & \omega^3_2 \\ \omega^3_2 & \omega^3_1 \end{pmatrix}$$

$$\tilde{C}^{(4)}_{a\sigma,b\lambda} = \begin{pmatrix} \omega^4_1 & \omega^4_2 \\ \omega^4_2 & \omega^4_1 \end{pmatrix}$$

$$\tilde{C}^{(5)}_{a\sigma,b\lambda} = \begin{pmatrix} \omega^5_{11} & \omega^5_{12} \\ \omega^5_{21} & \omega^5_{22} \end{pmatrix}$$

where

$$\omega^1 = d(1-d)\,\mathrm{circ}\Big[-(1-d)(1+4d)-d^2, \frac{1}{2}(1-d)(1+5d)+\frac{1}{2}d^2, \frac{1}{2}(1-d)(1+d)+\frac{1}{2}d^2, -(1-d)(1+2d)-d^2, \frac{1}{2}(1-d)(1+5d)+\frac{1}{2}d^2, \frac{1}{2}(1-d)(1+d)+\frac{1}{2}d^2\Big]$$

$$\omega^2 = \omega_1$$

$$\omega^3_1 = d(1-d)\,\mathrm{circ}\Big[-(1-d)(1+4d)-2d^2, \frac{1}{2}(1-d)(1+2d+3d^2)+d^3, \frac{1}{2}d(1-d)^2, 0, \frac{1}{2}d(1-d)^2, \frac{1}{2}(1-d)(1+2d+3d^2)+d^3\Big]$$

$$\omega^3_2 = d(1-d)\,\mathrm{circ}\Big[0, \frac{1}{2}d(1-d)^2, \frac{1}{2}(1-d)(1+2d+3d^2)+d^3, -(1-d)(1+4d)-2d^2, \frac{1}{2}(1-d)(1+2d+3d^2)+d^3, \frac{1}{2}d(1-d)^2\Big]$$

$$\omega_1^4 = d(1-d)\,\mathrm{circ}[-(1-d)(1+4d)-d^2, 0, (1-d)(1+4d)+4d^2, 0, (1-d)(1+4d)+4d^2, 0]$$

$$\omega_2^4 = d(1-d)\,\mathrm{circ}[0, (1-d)(1+4d)+4d^2, 0, -(1-d)(1+4d)-d^2, 0, (1-d)(1+4d)+4d^2]$$

$$\omega_{11}^5 = \mathrm{circ}[-2d(1-d), 0, -d(1-d), 0, -d(1-d), 0]$$

$$\omega_{12}^5 = \mathrm{circ}[0, d(1-d), 0, 0, 0, 0, d(1-d)]$$

$$\omega_{21}^5 = \omega_{12}^5$$

$$\omega_{22}^5 = \mathrm{circ}[-d(1-d), 0, 0, 0, 0, d(1-d)]$$

where circ designates a circulant matrix. (The arguments of circ are the elements of the first row of the matrix. Each subsequent row consists of the same elements cyclicly shifted right one column.)

Because of the rotational symmetry of the lattice and collisions, we can write a compact form for $\tilde{C}^{(0)}_{a\sigma,b\lambda}$,

$$\tilde{C}^{(0)}_{a\sigma,b\lambda} = \begin{pmatrix} C^{(0)}_{a1,b1} & C^{(0)}_{a1,b2} \\ C^{(0)}_{a2,b1} & C^{(0)}_{a2,b2} \end{pmatrix} = \sum_i \omega^{(i)}_{ab} \otimes \tau^{(i)}_{\sigma\lambda} \tag{31}$$

Here $\omega^{(1)}_{ab} = C^{(0)}_{a1,b1}$, $\omega^{(2)}_{ab} = C^{(0)}_{a1,b2}$, $\omega^{(3)}_{ab} = C^{(0)}_{a2,b1}$, and $\omega^{(4)}_{ab} = C^{(0)}_{a2,b2}$, and

$$\tau^{(1)}_{\sigma\lambda} = \begin{pmatrix} 1 & 0 \\ 0 & 0 \end{pmatrix}$$

$$\tau^{(2)}_{\sigma\lambda} = \begin{pmatrix} 0 & 1 \\ 0 & 0 \end{pmatrix}$$

$$\tau^{(3)}_{\sigma\lambda} = \begin{pmatrix} 0 & 0 \\ 1 & 0 \end{pmatrix}$$

$$\tau^{(4)}_{\sigma\lambda} = \begin{pmatrix} 0 & 0 \\ 0 & 1 \end{pmatrix}$$

We know that $\omega^{(i)}_{ab}$ are circulant matrices, having the form

$$\omega^{(i)}_{ab} = \mathrm{circ}[U^{(i)}_{11}, U^{(i)}_{12}, U^{(i)}_{13}, U^{(i)}_{14}, U^{(i)}_{15}, U^{(i)}_{16}]$$

where U_{1i} is an element of the circulant matrix. The eigenvalues of $\omega^{(i)}_{ab}$ are

$$\lambda^{(i)}_c = \sum_a U^{(i)}_{1a} \exp\left(\frac{2\pi i(c-1)(a-1)}{6}\right)$$

and

$$[\omega^{(i)}] \cdot \mathbf{v}^{(c)} = \lambda_c^{(i)} \mathbf{v}^{(c)} \tag{32}$$

where $i = 1,..., 6$ and $c = 1,..., 6$. The $\mathbf{v}^{(c)}$ are the eigenvectors. All the $[\omega^{(i)}]$ have the same eigenvectors.

Denoting $\tau^c_{\sigma\lambda}$ as

$$\tau^c_{\sigma\lambda} = \sum_i \lambda_c^{(i)} \tau^{(i)}_{\sigma\lambda} = \begin{pmatrix} \lambda^{c(1)} & \lambda^{c(2)} \\ \lambda^{c(3)} & \lambda^{c(4)} \end{pmatrix}$$

we have

$$\sum_\lambda \tau^c_{\sigma\lambda} W^{c,\mu}_\lambda = \xi^{c,\mu} W^{c,\mu}_\sigma \tag{33}$$

where $\xi^{c,\mu}$ and $W^{c,\mu}_\sigma$ are the eigenvalues and eigenvectors of $\tau^c_{\sigma\lambda}$, respectively.

We can write

$$f^{\lambda(1)}_b = \sum_c \psi^c_\lambda v^c_b \tag{34}$$

Thus,

$$\sum_{b,\lambda} \tilde{C}^{(0)}_{a\sigma,b\lambda} f^{\lambda(1)}_b = \sum_{\lambda,c} \psi^c_\lambda v^c_a \tau^c_{\sigma\lambda} \tag{35}$$

Since

$$\psi^c_\lambda = \sum_\mu \rho^{c,\mu} W^{c,\mu}_\lambda \tag{36}$$

by (33), we have

$$\sum_{b,\lambda} \tilde{C}^{(0)}_{a\sigma,b\lambda} f^{\lambda(1)}_b = \sum_{c,\lambda,\mu} \rho^{c,\mu} W^{c,\mu}_\lambda v^c_a \tau^c_{\sigma\lambda} = \sum_{c,\mu} v^c_a \xi^{c,\mu} W^{c,\mu}_\sigma \rho^{c,\mu} \tag{37}$$

The $\rho^{c,\mu}$ can be expressed as

$$\rho^{c,\mu} = \frac{1}{\xi^{c,\mu}} \sum_{a\sigma} (v^c_a W^{c,\mu}_\sigma)^0 L_{ia\sigma} \tag{38}$$

It is easy to decompose

$$\begin{aligned}
\rho^{c,\mu}(\text{visc}) &= -\frac{\beta_0}{2\xi^{c,\mu}} \sum_a (2\mathbf{e}_a \mathbf{e}_a - \hat{\mathbf{1}}) \sum_\sigma m_\sigma d_\sigma (1 - d_\sigma c^2_\sigma W^{c,\mu}_\sigma) : \nabla \mathbf{u} \\
\rho^{c,\mu}(\text{cond}) &= \frac{1}{\xi^{c,\mu}} \nabla \cdot \sum_a (v^c_a)^0 \mathbf{e}_a \sum_\sigma (W^{c,\mu}_\sigma)^0 c_\sigma d_\sigma \\
\rho^{c,\mu}(\nabla \cdot \mathbf{u}) &= -\frac{\beta_0}{2\xi^{c,\mu}} \left[\sum_a (v^c_a)^0 \right] \left[\sum_\sigma m_\sigma d_\sigma (1 - d_\sigma c^2_\sigma) \nabla \cdot \mathbf{u} \right]
\end{aligned} \tag{39}$$

We can obtain the first-order stress tensor

$$\Pi^{(1)}_{\alpha\beta} = \sum_{a,\sigma} m_\sigma (\mathbf{e}^\sigma_a)_\alpha (\mathbf{e}^\sigma_a)_\beta f^{\sigma(1)}_a$$

$$= \sum_{c,\mu} \left[\sum_a (\mathbf{e}^\sigma_a)_\alpha (\mathbf{e}^\sigma_a)_\beta v^c_a \right] \left(\sum_\sigma m_\sigma c^2_\sigma W^{c,\mu}_\sigma \right) [\rho^{c,\mu}(\text{visc}) + \rho^{c,\mu}(\nabla \cdot \mathbf{u})] \quad (40)$$

Note that the term $\rho^{c,\mu}(\text{cond})$ has no contribution to $\Pi^{(1)}_{\alpha\beta}$, and (40) can be rewritten as

$$\Pi^{(1)}_{\alpha\beta} = \frac{3\beta_0}{4} \sum_\mu \frac{1}{\xi^{3,\mu}} \left(\sum_\sigma m_\sigma c^2_\sigma W^{3,\mu}_\sigma \right) \sum_{\sigma'} d_{\sigma'}(1 - d_{\sigma'}) m_{\sigma'} c^2_{\sigma'} W^2_{\sigma'}$$

$$\times \left(\frac{\partial u_\beta}{\partial \alpha} + \frac{\partial u_\alpha}{\partial \beta} - \nabla \cdot \mathbf{u} \delta_{\alpha\beta} \right)$$

From the above equation, we obtain the shear viscosity

$$\mu_s = \frac{3\beta_0}{4} \sum_\mu \frac{1}{\xi^{3,\mu}} \left(\sum_\sigma m_\sigma c^2_\sigma W^{3,\mu}_\sigma \right) \sum_{\sigma'} d_{\sigma'}(1 - d_{\sigma'}) m_{\sigma'} c^2_{\sigma'} W^2_{\sigma'} \quad (41)$$

We also obtain an expression for the heat flux

$$\mathbf{q}^{(1)}_\alpha = \sum_{a,\sigma} c^3_\sigma (\mathbf{e}^\sigma_a)_\alpha f^{\sigma(1)}_a$$

$$= \sum_{a,\sigma} c^3_\sigma (\mathbf{e}^\sigma_a)_\alpha f^{\sigma(1)}_a(\text{cond})$$

$$= \sum_{c,\mu} \left[\sum_a (\mathbf{e}^\sigma_a)_\alpha v^c_a \right] \left(\sum_\sigma m_\sigma c^2_\sigma W^{c,\mu}_\sigma \right) \rho^{c,\mu}(\text{cond}) \quad (42)$$

or

$$\mathbf{q}^{(1)}_\alpha = \frac{2}{\xi^{2,2}} \left(\sum_\sigma m_\sigma c^3_\sigma W^{2,2}_\sigma \right) \left(\sum_{\sigma'} c_{\sigma'} W^{2,2}_{\sigma'} \right) \left(\frac{\partial d_\sigma}{\partial \varepsilon} \right)_\rho \frac{\partial \varepsilon}{\partial \alpha} = -\lambda \frac{\partial \varepsilon}{\partial \alpha}$$

We obtain the following analytical formula for heat conductivity:

$$\lambda = -\frac{3}{\xi^{2,2}} \left(\sum_\sigma m_\sigma c^3_\sigma W^{2,2}_\sigma \right) \left(\sum_{\sigma'} c_{\sigma'} W^{2,2}_{\sigma'} \right) \left(\frac{\partial d_\sigma}{\partial \varepsilon} \right)_\rho \quad (43)$$

The derivative $(\partial d_\sigma / \partial \varepsilon)_\rho$ in (43) can be evaluated from the definitions (3) (5). Following the method proposed by Hatori and Montgomery,[14]

after tedious algebra, we can obtain the kinematic viscosity $\nu = \mu/n$ and conductivity λ as follows:

$$\begin{aligned} \nu &= -\frac{1}{16}\left(\frac{9}{\xi^{3,1}} + \frac{1}{\xi^{3,2}}\right) - \frac{5}{16} \\ \lambda &= -\frac{819d}{176\xi^{2,2}} \end{aligned} \tag{44}$$

where

$$\begin{aligned} \xi^{3,1} = &-11d + 38d^2 + 6d^3 - 351d^4 + 762d^5 + 132d^6 - 2925d^7 + 4347d^8 \\ &- 360d^9 - 6390d^{10} + 8748d^{11} - 5508d^{12} + 1728d^{13} - 216d^{14} \\ \xi^{3,2} = &-3d(1-d)^3 - 12d^2(1-d)^2 - 3d^3(1-d) \end{aligned}$$

and

$$\begin{aligned} \xi^{2,2} = &-6d + 7d^2 + 31d^3 - 115d^4 + 118d^5 \\ &+ 123d^6 - 494d^7 + 636d^8 - 432d^9 + 156d^{10} - 24d^{11} \end{aligned}$$

The constant in (44), 5/16, is the lattice viscosity, the second-order correction term to the kinetic equation (2). It is a discrete effect of the lattice, and is 2.5 times larger than that found in the FHP unit-mass single-speed models.[12] In Figs. 2 and 3, we present the viscosity and heat conductivity as a function of reduced density. They are always positive. The viscosity has a shape similar to other FHP models. Using the same method discussed above, the general viscosity for different d_σ can also be worked out immediately by allowing $\omega_{ab}^{(i)}$ in (31) to be σ-dependent.

The complete equations for momentum and energy up to $O(u^2)$ now have the following form:

$$\begin{aligned} \partial_t(n\mathbf{u}) + \nabla\cdot(ng(n,\varepsilon)\,\mathbf{uu}) &= -\nabla p + \nabla\cdot(\mu\nabla\mathbf{u}) \\ \partial_t(n\varepsilon) + \nabla\cdot(n\varepsilon\mathbf{u}) &= -\nabla\cdot(nh(n,\varepsilon)\,\varepsilon\mathbf{u}) - p\nabla\cdot\mathbf{u} \\ &\quad + \nabla\cdot(\lambda\nabla\varepsilon) + \mu\nabla\mathbf{u}:\nabla\mathbf{u} \end{aligned} \tag{45}$$

The classical thermohydrodynamic equations[15] are recovered for $g = 1$ and $h = 0$ in (45).

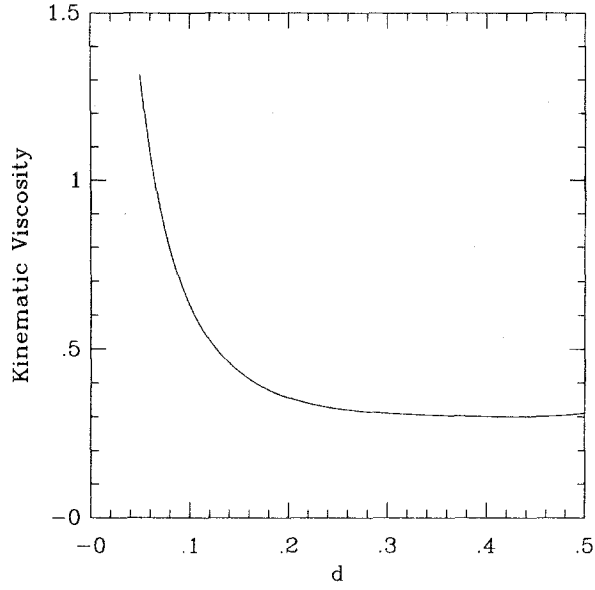

Fig. 2. Kinematic viscosity versus reduced density d for the present model with $d = d_0 = d_1 = d_2$.

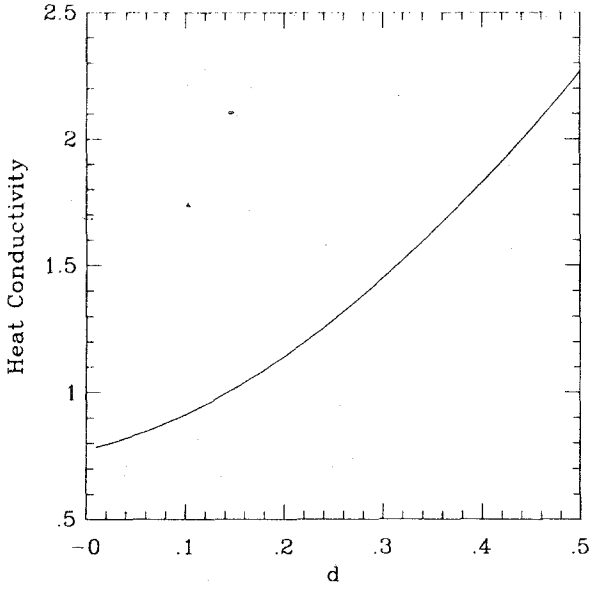

Fig. 3. Heat conductivity versus reduced density d for the present model with $d = d_0 = d_1 = d_2$.

4. HEAT CONDUCTION IN CHANNEL FLOWS

4.1. Thermal Boundary Implementation

The thermohydrodynamic equations (45) can be used to simulate physical systems with temperature-dependent boundaries. At these boundaries, appropriate collision rules must be chosen.

Adiabatic and isothermal boundary conditions are commonly used. Adiabatic conditions require zero temperature gradient normal to the wall. In a lattice gas model, this is achieved by selecting incident and reflected particles which have the same kinetic energy (mirror reflection), i.e., there is no change in type of particles at the wall. A constant-temperature boundary can be obtained by maintaining a fixed ratio between speed-one and speed-two particles after a collision with the wall. For example, a high-temperature boundary can be achieved by allowing a speed-one particle to have a nonzero transition probability to become a speed-two particle.

There are two commonly used velocity boundary conditions: nonslip and free-slip. The nonslip condition produces zero velocity at the wall. This is called a bounce-back condition. The free-slip velocity condition is useful for thermohydrodynamic problems. Here we require the velocity derivative normal to the wall to be zero. The velocity tangential to the wall remains unchanged. This is sometimes called the free-slip boundary condition. Adiabatic and isothermal boundary rules must conserve mass and satisfy some velocity restrictions. Since speed-one and speed-two particles in our model do not have the same mass, we cannot simply just change the speed of the particles and still conserve mass. A simple way to reduce the temperature and conserve mass is to allow two speed-two particles which occupy the same boundary site to become one speed-one particle. The inverse process can be used to raise the boundary temperature. When all particles in the system have zero speed, the system has zero temperature. When all particles are speed-two particles and the macroscopic velocity is zero, the system will have the maximum temperature, $\varepsilon = 2$.

4.2. Heat Conduction

A typical two-dimensional heat conduction problem is to determine the temperature field between two plane plates with a small temperature difference. When the macroscopic velocity is zero, the temperature is a linear function of the distance from one plate for time $t \to \infty$. A simulation of this system was run using a periodic condition, $N_i^{\sigma}(0, t) = N_i^{\sigma}(L_x, t)$, where L_x is the x-direction length (along the channel). The initial condition is constant temperature everywhere ($\varepsilon = 6/7$) and we use a reduced density

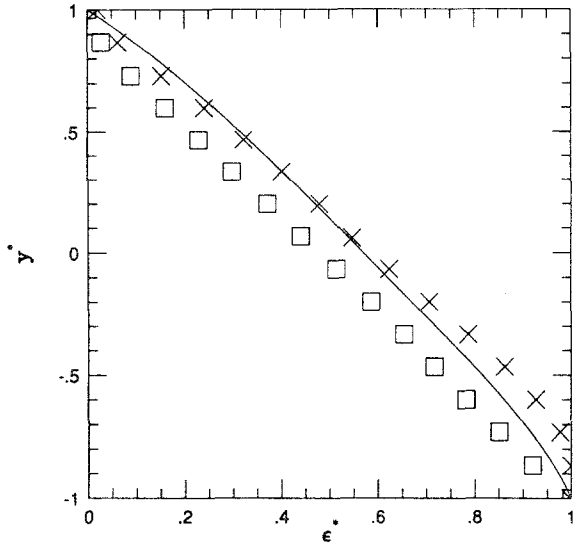

Fig. 4. The comparison of the temperature distribution across the channel width when the system has and does not have a net flow along the x direction. (×) The temperature for the system with an x-direction flow ($B_r = 0.21$). (□) The temperature for the system with zero net flow ($B_r = 0$). The solid line is the analytical result in (46) for $B_r = 0.21$.

d of 0.25 for all directions. The lower wall has a hot temperature of 1.13 and the upper wall has the lower temperature of 0.85. The simulation occupies 512×256 lattice sites. We have used a 512×4 site average to obtain temperatures as the function of y. In Fig. 4, we present the temperature distribution (□ symbols) for time step 30,000. The normalization is the same as in Section 4.3.

4.3. Heat Conduction in a Channel Flow with a Poiseuille Velocity Profile

An interesting simulation was done for the system described in Section 4.2 but with forcing in the x direction. This forcing is obtained by flipping particle velocities along the flow direction. Because speed-one and speed-two particles have the same momentum, we can use the same forcing for both types of particles. There are two allowed forcings in the x direction: a particle along the direction of 120° with the x axis changes to be a particle along the direction of 60° with x axis. The reflection of this flipping through the x axis is also allowed. This flipping process does not change total mass or total energy; only the momentum changes. In a constant-temperature system, the momentum increase is balanced by friction at the

wall. The system relaxes to a parabolic velocity profile. If the system has a temperature gradient and the transport coefficient is independent of temperature, the momentum equation still has the same form as the constant-temperature case, but the temperature equation will couple with the velocity distribution. We define

$$u^* = \frac{u}{U_0}, \qquad y^* = \frac{y}{h}$$

$$\varepsilon^* = \frac{\varepsilon - \varepsilon_0}{\varepsilon_1 - \varepsilon_0}$$

where ε_0 and ε_1 are the upper wall and lower wall temperatures, respectively, $2h$ is the channel width, and U_0 is the maximum velocity in the channel center ($y = 0$). Then, we have a parabolic velocity distribution:

$$u^* = (1 - y^{*2})$$

From (45), we have the temperature equation

$$\frac{d^2\varepsilon^*}{d^2y^*} = -B_r \left(\frac{du^*}{dy^*}\right)^2$$

where $B_r = \mu U_0^2/\lambda(\varepsilon_1 - \varepsilon_0)$ is the Brinkman number, which is the product of the Prandtl number and Eckert number.[16] It can be shown that the temperature has the following distribution:

$$\varepsilon^* = \frac{B_r}{3}(1 - y^{*4}) + \frac{1}{2}(1 - y^*) \tag{46}$$

In Fig. 4, we present simulation results (×) compared with the analytic temperature distribution (46) (solid line) for $U_0 = 0.267$ ($B_r = 0.21$). The squares in the plot represent the simulation results for $B_r = 0$. The numerical results of the temperature distributions agree qualitatively with (46) except for boundary regions. This disagreement may represent the effect of the variation of the transport coefficients in the present model when a temperature gradient exists.

5. BÉNARD CONVECTION

Bénard convection is perhaps the best-studied hydrodynamic instability problem because in this process a simple instability mechanism produces complicated flow patterns. Again we consider fluid flow between

two plane plates with different temperatures as described in Section 4. But now we impose a large temperature difference. For comparison with other data, in this section we use T instead of ε. The gravitational forcing is here in the negative y direction. The transition from conduction to convection, determined in the linear stability analysis, depends on the Rayleigh number:

$$Ra = \frac{\alpha n \, \Delta T \, L_y^3 f}{\lambda \nu} \tag{47}$$

where α is the coefficient of thermal expansion, $-(1/n)\,\partial n/\partial T$, and ΔT is the temperature gradient between two plates; f is the forcing rate per unit area per time step; L_y is the distance between two plates; λ is the thermal conductivity; and ν is the kinematic viscosity. The Boussinesq approximation is needed to derive the approximate equation for the small-gradient case. This approximation assumes that convection can be described by the incompressible Navier–Stokes equation and that the density in the forcing term nf can be replaced by $n = n_0(1 - \alpha \, \Delta T)$. In an ideal gas system $\alpha = 1/T$.

The system size in our simulation is fixed to make L_x, the lattice size in the x direction, twice the size of L_y. This allows the system to support the typical convection cells seen in experiments.[17] The velocity boundary will affect the critical Rayleigh number. The free-slip boundary condition has a higher critical Rayleigh number. We use both nonslip and free-slip boundary conditions to determine their effects on the formation of the convection cells. The initial condition we use is zero velocity. The reduced density for the initial time step is $d_0 = d_1 = d_2 = 0.25$.

Because the lattice gas system itself has considerable internal noise, it is difficult to determine precisely the critical Rayleigh number for the transition from conduction to convection. The measurement of the Nusselt number as a function of Rayleigh number determines how the heat flux and heat conductivity change when Ra is varied. The critical point can be determined from these measurements. Here $Nu = \lambda_{\text{eff}}/\lambda$, the ratio of the effective conductivity λ_{eff} to the conductivity λ for $v_y = 0$. The λ_{eff} can be measured using the following relation:

$$q_y = -\lambda_{\text{eff}} \frac{\Delta T}{\Delta y} \tag{48}$$

Here q_y is the heat flux determined from the microscopic measurement using $q_y = \sum_{a,\sigma} m_\sigma f_a^\sigma (\mathbf{e}_a^\sigma - \mathbf{u})^2 \, (\mathbf{e}_a^\sigma - \mathbf{u})_y$. Because the Ra number varies as L_y^3, it is easy to use L_y to vary Ra. The forcing scheme is very similar to that described in Section 4. But this forcing is not the same as a gravity.

For identical molecules in a uniform gravitational field, all particles in space at each time step experience the same acceleration. In a lattice gas, however, a particle only can accept a unit momentum by changing its direction. If all particles at each time step are accelerated, the forcing will be too strong. A random, low-frequency particle forcing is required. The forcing sites used in this paper are randomly distributed in space and time rather than using fixed space points.[10] For a given flipping rate, it is difficult to make the forcing directly proportional to density n as required by linear stability theory, because of exclusion of multiple particle occupations For example, suppose we find a particle in the b direction in Fig. 1, which should change it to be in the f direction, but if there is a particle in the same cell in the f direction, the forcing is prohibited. Thus this acceleration is actually proportional to $d(1-d)$, where d is the reduced density. Suppose that $d=d_0(1+\alpha\,\Delta T)$, where d_0 is the reduced density for the constant-temperature system, then we have

$$d(1-d)=(d_0-d_0^2)+\alpha d_0(1-2d_0)\,\Delta T+o(\Delta T^2)$$

The constant term can be combined with the pressure gradient term and the ΔT term is the Boussinesq force and there is only a rescaling effect compared with the force proportional to density. In order to keep the coefficient of ΔT positive, the reduced density must be less than half. This same restriction is required in order to keep $g(n)$ positive.

In Fig. 5, we present typical lattice gas simulation results for the convection cells. The system size is 512×256 lattice sites. The initial density

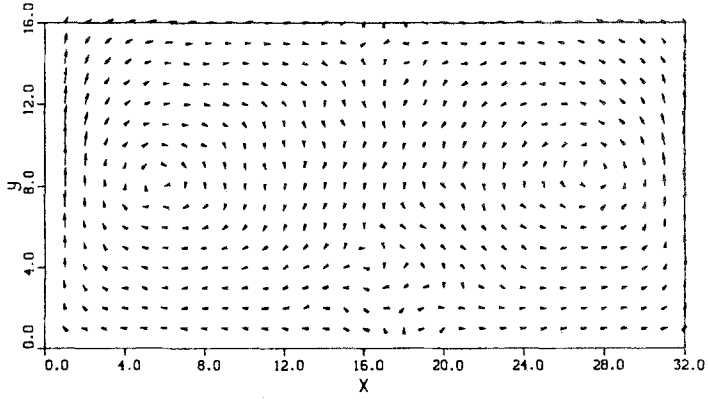

Fig. 5. Velocity vector distribution in Bénard convection. The bottom boundary has a temperature of 1.48 and the upper boundary has a temperature of 0.54. The left and right boundaries are adiabatic, with a free-slip velocity condition being used for tangential velocity components.

and velocity loading is random. After about 30,000 times steps, we time average for 3000 steps. A spatial average of 16×16 sites is used to obtain a macroscopic value. Then we can have 32×16 macroscopic sites. A nonslip condition for all walls and an adiabatic thermal condition for the left and right boundaries have been used. Two convection vortices are observed. These two vortices are not completely stable. The centers of the vortices oscillate slightly about the center point. There are several causes for this. First, the Rayleigh number is above the transition point. Second, the forcing mechanism used is impulsive and random. This generates local noise which destabilizes the vorticity pattern. Third, the convection coefficients $g(n, T)$ in the momentum equation and $h(n, T)$ in the energy equation differ. This causes different time scales for the two equations.

When we use a periodic condition in the lateral direction and keep the upper and lower boundaries as before and change the wall to nonslip conditions, all simulations show similar spatial velocity structures, but with a minor perturbation of the vortex center. Figures 6 and 7 are the density and temperature contours for Fig. 5. Typical convection behavior is found. In Fig. 8, we give the temperature (averaged along the x direction) profiles from Fig. 7. This plot shows that there is a thermal boundary near the upper and bottom boundaries. The density distribution has a structure that agrees with other simulations.[18]

The measurement of heat flux in the y direction q_y (which should be linearly proportional to the Nusselt number) versus temperature difference ΔT (which should be linearly proportional to Ra) is presented in Fig. 9. The forcing rate for each time step is about 10 and the average density per

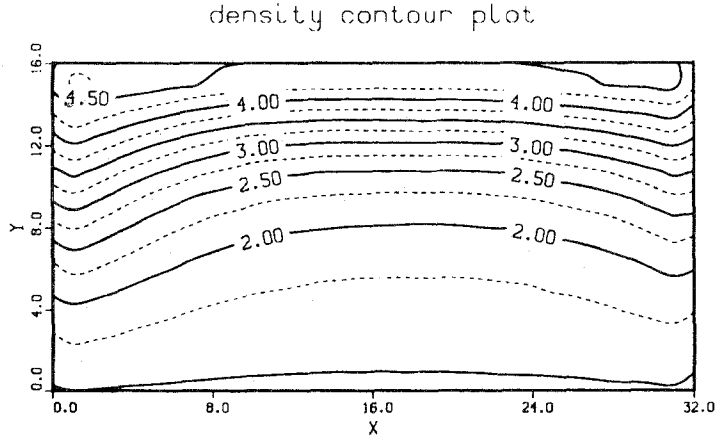

Fig. 6. Density contours from the lattice gas simulation for Fig. 5.

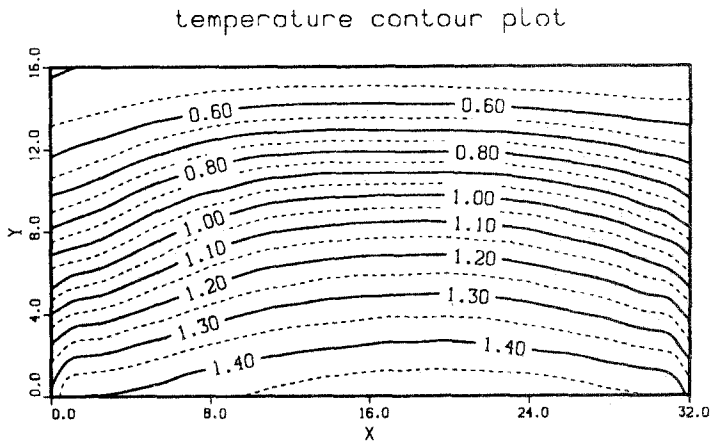

Fig. 7. Temperature contours from the lattice gas simulation for Fig. 5.

cell is 3.25. After the system approaches a local equilibrium, a spatial average over 1000 time steps was used to obtain the heat flux. An almost parabolic relation between heat flux and temperature difference for ΔT is found. This means that the effective conductivity λ_{eff} will be linearly proportional to ΔT. This agrees with experimental observations.[17] The

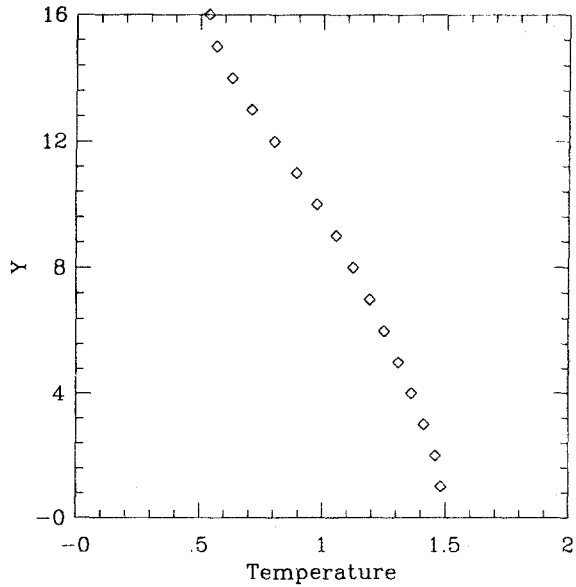

Fig. 8. The temperature profile obtained by averaging over x for Fig. 7.

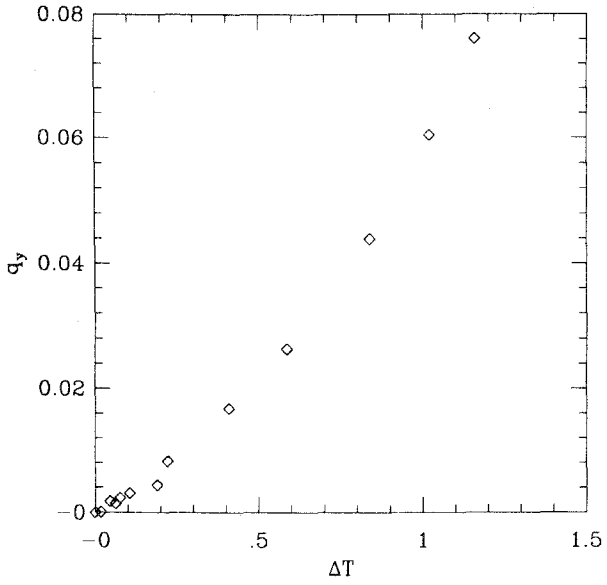

Fig. 9. Heat flux versus temperature difference between two plates.

change in heat flux with a change of temperature in experiments has a sharp change of slope at the critical Rayleigh number. Our simulation does not clearly present this phenomenon. Noise in the lattice gas model is possibly too large. An extrapolation gives a transition point at $\Delta T = 0.3$, which corresponds to a Rayleigh number of 2508.

6. ISOTHERMAL PROBLEMS AND GALILEAN INVARIANCE

Now we consider the isothermal incompressible fluid limit for the present model. We want to recover the Navier–Stokes equation with no unphysical terms at some fixed temperatures. Note that if ε and n both are constant, the energy equation is automatically satisfied. Mass density n and energy ε are defined by (3) and (5). Thus, for a given mass density, we can vary the temperature by varying the ratios of different types of particle to mass density $k_\sigma = d_\sigma/n$. The temperature is determined by these ratios. The quantities d_σ we consider here are the equilibrium values, determined by Eq. (13).

If the particles are in statistical equilibrium, the collisions between the different types of particles should satisfy the detailed balance condition. After eliminating α_0 and γ_0 in (11) for the zero-velocity case, we obtain

$$\bar{d}_i^x \bar{d}_k^y = \bar{d}_j^z \tag{49}$$

as required by the principle of detailed balance. Here

$$\bar{d}_i = \frac{d_i}{1-d_i}, \qquad x = \frac{1}{m_i(\varepsilon_i - \varepsilon_j)}, \qquad y = \frac{1}{m_k(\varepsilon_i - \varepsilon_k)}, \qquad z = \frac{1}{m_i}\left[\frac{1}{\varepsilon_j - \varepsilon_k} + \frac{1}{\varepsilon_i - \varepsilon_j}\right]$$

Together with Eqs. (3) and (5), we have four variables, d_0, d_1, d_2, and ε, but only three equations. The internal energy can be treated as a free parameter in the isothermal limit. We may add the equation $g(n, \varepsilon) = 1$, or equivalently, $p_1 = 0$, and ask whether physical solutions exist for these equations. Physical solutions require $1 \geqslant d_\sigma \geqslant 0$ and $\varepsilon_{\max} \geqslant \varepsilon \geqslant 0$. Here σ varies from 0 to $N-1$ and $\varepsilon_{\max}$ is determined by the geometry. For physical solutions, we may write $d_\sigma = d_\sigma(n)$ and $\varepsilon = \varepsilon(n)$. We show later that physical solutions exist. Because the lattice gas model has density fluctuations, we cannot exactly satisfy $g(n, \varepsilon) = 1$. Instead, we can write down the velocity dependence of $n = n_0 + n_1 u^2$ and $\varepsilon = \varepsilon_0 + \varepsilon_1 u^2$ for small macroscopic velocities. Consequently, we have $g(n, \varepsilon) = 1 + O(u^2)$ and $p_1 = O(u^2)$. One can show that these u^2 corrections contribute terms of order u^4 to the Navier Stokes equation. Hence, the order of accuracy of the Navier Stokes equation is unchanged by corrections of order u^2 in the density and internal energy.

To illustrate this idea, to the second order in $|\mathbf{u}|$, we obtain the equilibrium distributions d_0, d_1, and d_2 and the energy ε as a function of density n. We solve for these four variables using the four equations

$$\begin{aligned} \frac{3}{2} d_0 + 6d_1 + 3d_2 &= n \\ 3d_1 + 6d_2 &= n\varepsilon \\ \left(\frac{1-d_1}{d_1}\right)^2 &= \left(\frac{1-d_0}{d_0}\right)\left(\frac{1-d_2}{d_2}\right) \\ nd_1(1-d_1)(1-2d_1) + 2d_2(1-d_2)(1-2d_2) &= 12[d_1(1-d_1) + d_2(1-d_2)]^2 \end{aligned} \tag{50}$$

In Fig. 10, we present the numerical solution of d_0, d_1, and d_2 for $n \leqslant 2.5$. Other allowed physical solutions appear for $3 \leqslant n \leqslant 4.5$ and $7 \leqslant n \leqslant 10.5$. For the excluded values of n, at least one d_i becomes unphysically negative.

In Fig. 11, the solid line shows those values of ε and n for which $g = 1$. Physical solutions exist along this line. We also plot the physically allowed $\varepsilon(n)$ for other values of g. There are two reasons to be interested in the dependence of the solution on g. First, one would like $\varepsilon(n)$ to be a slowly varying function of g, so that small density fluctuations cause small changes in g. We see that this is true. Second, we could carry out the usual g-scaling

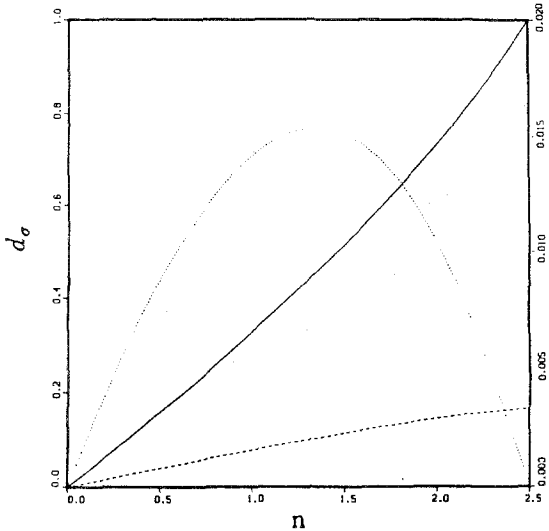

Fig. 10. Equilibrium distributions for speed-zero (solid line), speed-one (dashed line), and speed-two particles (dots, right vertical coordinate) when $g(n, \varepsilon) = 1$. This figure demonstrates the existence of physical solutions when g, the coefficient of the $\mathbf{u} \cdot \nabla \mathbf{u}$ term, is unity.

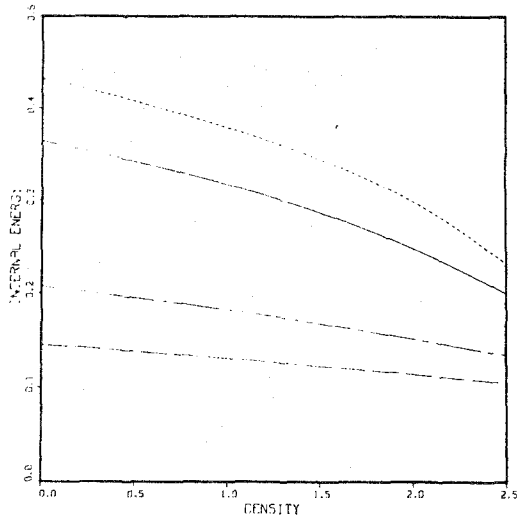

Fig. 11. $\varepsilon(n)$ plots for (- -) $g = 0.9$, (—) 1.0, (···) 1.2, (- — -) 1.5, and (· — ·) 2.0. This figure illustrates a range of g for which physical solutions exist.

of time, viscosity, and pressure, and obtain a corresponding change in the Reynolds number, $Re = gul/v$. Here u is a characteristic velocity, l is a characteristic length, and v is the viscosity. In previous calculations, g is about 1/3. Having $g = 1$ allows at least a factor-of-three higher Reynolds number. Letting g be larger than one and scaling allows even higher Reynolds numbers for the same viscosity. This Reynolds number increase is important because the computer time for a lattice gas calculation depends on the fourth power of the Reynolds number.

In order to demonstrate the modified $g(n)$ effect in the equation of state, in Fig. 12 we present computational results for the 13-bit model for the energy decay in Kolmogorov flow, compared with analogous results for the FHP-I model.[19,20] A system size of 4096×4096 lattice sites was used for both cases. The period in the y direction is $4096 \times \sqrt{3}/2$ lattice units. Momentum and energy have been averaged over 64×64 lattice sites to obtain 64×64 macroscopic points. The streamwise energy of the system is obtained by summing over all the macroscopic streamwise kinetic energies. There is a substantial energy oscillation in FHP-I model because of the $g(n)$ effect in the equation of state. We find that the oscillation in kinetic

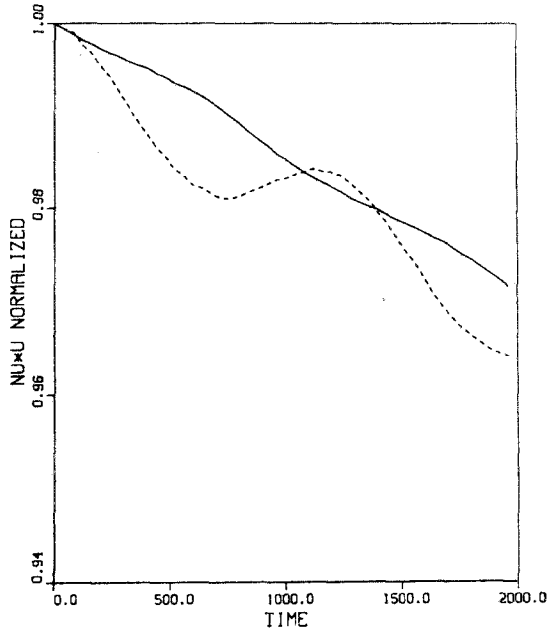

Fig. 12. The streamwise kinetic energy for the Kolmogorov flow, $u_0 = 0.3 \sin(y)$. The solid curve is the 13-bit result with $n = 2.0$ and $\varepsilon = 0.25$. The dashed curve is the six-bit result when $n = 1.8$ and $\varepsilon = 0.5$. The unphysical oscillation presented in the six-bit result is reduced significantly in the 13-bit result because the u^2 term in the pressure has been eliminated.

energy decay greatly decreases for the present model because p_1 equals to zero. The initial velocity is $u_0 = 0.3 \sin(y)$. The initial conditions for the 13-bit model are $n = 2.0$ and $\varepsilon = 0.25$; for FHP-I, $n = 1.8$ and $\varepsilon = 0.5$. The internal energy decay rate is within 3% of the theoretical prediction.

The detailed-balance condition in (49) requires some modification if the temperature and density changes are not small, as expected in compressible cases for moderate velocities. For these cases, one may introduce the parameter γ, which is the ratio of the probability of a collision process to the probability of its inverse process. γ is one for the present model. Therefore, the equilibrium distribution of (11) should include a potential energy depending on γ. Equation (49) will then be replaced by another equation which contains a γ dependence.

7. CONCLUDING REMARKS

In this paper, we have presented a lattice gas model with 13 discrete velocities for simulating thermohydrodynamics. An analytical derivation shows that this model obeys the compressible Navier–Stokes equations. Simulations confirm the usefulness of the model for thermohydrodynamic flow problems. Applications of the model to typical thermal problems have produced results which compare well with other numerical and analytic results.

The collision operations used in this paper are not optimized. In order to obtain a larger Reynolds number, we can include all allowed collision processes. Because we can vary $g(n)$ in the system for isothermal systems, it is possible to obtain a large R_* (ref. 2) by optimizing the collision operator and choosing an optimal density and temperature domain.

The generalization of the results of this paper to three-dimensional thermohydrodynamics is expected to be straightforward.[21]

Further studies and applications of this model are in progress. First, the success of this model in recovering Galilean invariance at a particular temperature and density make it plausible that we can use a system with many discrete velocities to obtain a more general Galilean invariance without the isothermal restriction. It will be interesting to address such questions as: how many speeds are needed to recover the Galilean invariance and to obtain a correct equation of state without velocity dependence? Second, there are many interesting theoretical and engineering problems which can be simulated using this lattice gas model, including flow through porous media, mantle convection, and biological flows. The viscosity of the present model depends on the local temperature and density. This is an important property for simulating realistic materials in mantle convection.[22] In general, these flows have low Reynolds number

and complicated boundaries. Third, the extension of this model to include other properties, such as chemical reactions and phase transitions, is possible.

Studies by Nadiga *et al.*[23] have shown how many speeds are required to reproduce specific physical phenomena, including shocks and equilibrium Maxwellian distributions.

ACKNOWLEDGMENTS

We thank David K. Campbell, Kenneth Eggert, Robert Ecke, Darlou Lee, William Matthaeus, Tim Sullivan, Bryan Travis, Hua Zao, and Fang Zhong for helpful discussions. This work was supported by the U.S. Department of Energy at Los Alamos National Laboratory, by DARPA grant DPP88-50, and by the NASA Innovative Research Program under grant NAGW-1648.

REFERENCES

1. U. Frisch, B. Hasslacher, and Y. Pomeau, *Phys. Rev. Lett.* **56**:1505 (1986).
2. U. Frisch, D. d'Humières, B. Hasslacher, P. Lallemand, Y. Pomeau, and J.-P. Rivet, *Complex Systems* **1**:649–707 (1987).
3. S. Chen, K. Diemer, G. D. Doolen, K. Eggert, C. Fu, S. Gutman, and B. Travis, Lattice gas automata for flow through porous media, *Physica D* (1990), in press.
4. A. Lawniczak, D. Dab, R. Kapral, and J. P. Boon, Reactive lattice gas automata, *Physica D* (1990), in press.
5. H. Chen, S. Chen, G. D. Doolen, Y. C. Lee, and H. A. Rose, *Phys. Rev. A* **40**:2850 (1989).
6. A. Cécile and S. Zaleski, *Phys. Rev. Lett.* **64**:1 (1990).
7. D. H. Rothman and J. M. Keller, *J. Stat. Phys.* **52**:1119 (1989).
8. L. Luo, H. Chen, S. Chen, G. D. Doolen, and Y. C. Lee, Relaxation processes in lattice gas automata, preprint (1990).
9. D. Frenkel and M. H. Ernst, *Phys. Rev. Lett.* **63**:2165 (1989).
10. C. Burgess and S. Zaleski, *Complex Systems* **1**:31 (1987).
11. S. Wolfram, *J. Stat. Phys.* **45**:471 (1986).
12. D. d'Humières and P. Lallemand, *Complex Systems* **1**:599 (1987).
13. H. Chen and W. H. Matthaeus, *Phys. Fluids* **30**:1235 (1987).
14. T. Hatori and D. Montgomery, *Complex Systems* **1**:735 (1987).
15. K. Huang, *Statistical Mechanics* (Wiley, New York, 1987).
16. M. White, *Viscous Fluid Flow* (McGraw-Hill, 1974).
17. G. Ahlers, Experiments on bifurcations and one-dimensional patters in nonlinear systems far from equilibrium, *Lectures in the Sciences of Complexity*, D. Stain, ed. (Addison-Wesley, 1989), p. 175.
18. J. A. Given and E. Clementi, *J. Chem. Phys.* **90**:7376 (1989).
19. J. P. Dahlburg, D. Montgomery, and G. Doolen, *Phys. Rev. A* **36**:2471 (1987).
20. S. Chen, Z. She, L. C. Harrison, and Gary D. Doolen, *Phys. Rev. A* **39**:2725 (1989).

21. K. Molvig, P. Donis, J. Myczkowski, and G. Vichniac, Removing the discrete artifacts in 3D lattice gas fluids, in *Discrete Kinetic Theory, Lattice Gas Dynamics and Foundation of Hydrodynamics*, R. Monaco, ed. (World Scientific, 1989), p. 409.
22. U. R. Christensen, Heat transport by variable viscosity convection and implications for the earth's thermal evolution, preprint.
23. B. T. Nadiga, J. E. Broadwell, and B. Sturtevant, Study of multipeed cellular automaton, in *Rarefied Gas Dynamics: Theoretical and Computational Techniques*, E. P. Muntz, D. P. Weaver, and D. H. Campbell, eds. (AIAA, Washington, D.C., 1989), pp. 155–170.